Title: Emergent honeycomb topology of the leaf spongy mesophyll

Authors: Aleca Borsuk[1*], Adam Roddy[1], Guillaume Théroux-Rancourt[2], Craig Brodersen[1]

Affiliations:

[1] School of Forestry & Environmental Studies, Yale University, New Haven, CT, 06511, USA.

[2] Institute of Botany, University of Natural Resources and Life Sciences Vienna, Austria.

*Correspondence to: aleca.borsuk@yale.edu

Abstract: The spongy mesophyll layer in leaves is ubiquitous among vascular plants, yet its structural characterization is typically described as a disordered assemblage of isodiametric cells. We characterized spongy mesophyll among diverse taxa using X-ray microCT imaging and found that leaves with small cell sizes, high cell packing densities, and close vein spacing were congruent with the isodiametric paradigm and optimized for CO_2 absorption. When these structural traits exceed well-defined thresholds, the spongy mesophyll was instead organized according to simple allometric scaling rules at the cellular level, with an emergent topological motif of an irregular honeycomb that obeys Euler's Law of space filling at the tissue level and minimizes cellular investment. Our data suggest two distinct topological classes based on the optimization of the spongy mesophyll for either photosynthetic performance or minimal resource investment.

One Sentence Summary: Three-dimensional imaging reveals conserved structural motifs in the landscape of the inner leaf.

Main Text:

The laminar leaf with reticulate venation is ubiquitous among terrestrial vascular plants, and convergence on this form has occurred independently in at least four distinct lineages since the Paleozoic (*1*). Despite the structural diversity and the range in size associated with leaf form (*2*), the interior of most laminar leaves has a conserved morphological scheme consisting of two photosynthetic layers arising from a common dorsiventral developmental framework (*3*): the palisade and the spongy mesophyll. The palisade mesophyll is generally positioned immediately below the upper epidermis and is composed of cylindrically shaped cells oriented perpendicular to the leaf surface. This layer is characterized by a high surface area to volume ratio that facilitates CO_2 absorption in a region of the leaf where light is abundant and photosynthetic rates are high (*4–7*). The spongy mesophyll, positioned below the palisade, is generally treated as a disordered and loosely packed assemblage of isodiametric, or roughly spherical, cells. It is thought that this tissue satisfies multiple biophysical roles (*8*), and helps to increase both light scattering and CO_2 conductance from the stomata in the lower epidermis to the palisade (*9*, *10*). However, testing such hypotheses requires detailed structural characterization that has been difficult to achieve due to the scale, complexity, and three-dimensional (3D) organization of the spongy mesophyll (*11*). Although specific examples of spongy mesophyll cells deviating from the isodiametric shapes to which they are typically assumed to conform have been reported (*8*, *12–15*), limited data exists on the general principles in structural organization of this tissue or how structural variation influences leaf function. Thus, we sought to determine the 3D geometry of spongy mesophyll using X-ray microCT imaging, to investigate the variance in spongy mesophyll architecture, to initiate an understanding of how variation arises, and to explore relationships between these structural properties and critical leaf traits at multiple scales of

functional derivation, i.e. spongy mesophyll surface area to volume ratio (SA_{mes}/V_{mes}), leaf photosynthetic capacity (A_{max}), and optimality of resource allocation.

Structural characterization

Using X-ray micro-computed tomography (microCT) imaging (*5*, *11*, *16*) we extracted 3D anatomical traits of the spongy mesophyll for 40 species with laminar leaves and reticulate venation that represented every major clade of terrestrial vascular plants, with several congeneric pairs for deeper investigations into the extent of variation between closely related species (Data Set S1). This analysis revealed two dominant spongy mesophyll classes (Fig. 1) with low topological diversity across the sampled species. Spongy mesophyll class was defined by its organization in the paradermal plane, i.e. parallel to the leaf surface. In the first class (27% of the species), spongy mesophyll conformed to the established isodiametric model, and was composed of a network of interconnected small-diameter cells surrounded by continuous intercellular airspace (IAS; Fig. 1A,B; *16*). This class of spongy mesophyll has a disordered 3D network best described as an open cell foam (*17*).

In contrast, spongy mesophyll in the second class was composed of layers of mesh-like cellular tissue that filled space in a manner that conformed to the topological principles governing a honeycomb (Fig. 1C,D). The honeycomb topology was present in 72.5% of the species sampled (21 of 30 genera). Congeneric sampling revealed that spongy mesophyll topology is conserved within the genus for our dataset (Data Set S1). While we restricted our analysis to the former two groups for species with reticulate venation, we note that deviation from those two classes occurred, including in spinach (*Spinacia oleracea*, Fig. S1A) with highly elongated cells forming large and continuous airspace volumes, and in the aquatic water lily, *Nuphar polyespela*, with elongated chambers presumably to increase the air-space volume

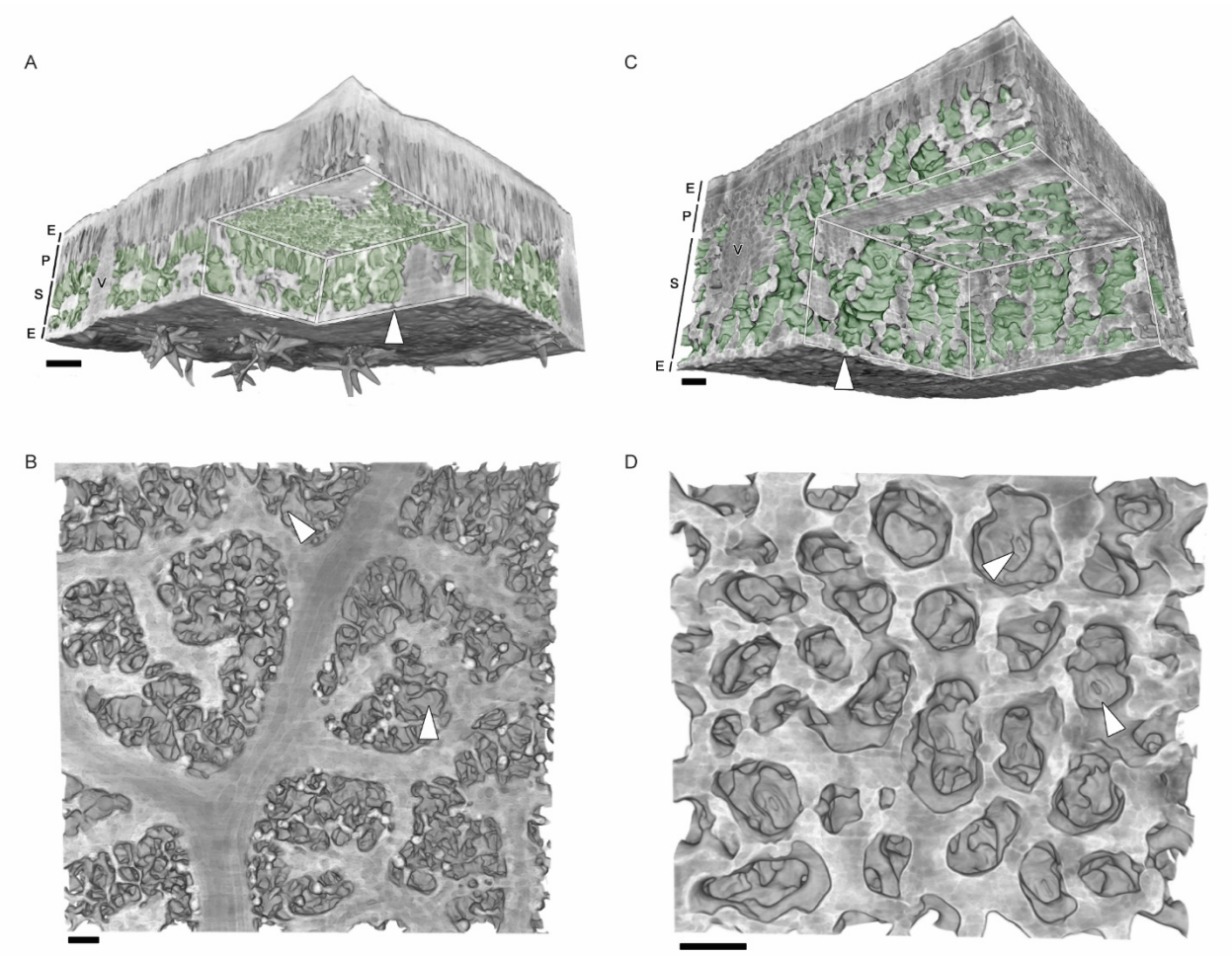

Fig. 1. 3D views of the two primary topological classes of spongy mesophyll imaged with microCT. (A) Representative leaf with the non-honeycomb spongy mesophyll (*Quercus suber*) with cropped interior showing intercellular airspaces (green) within an irregular network of spongy mesophyll (S). Epidermis (E), palisade mesophyll (P), and vascular tissue (V) shown in grayscale. Stomate indicated by the white arrow. Scale bar = 50 µm. **(B)** Paradermal view of the same *Q. suber* leaf's spongy mesophyll and veins. **(C)** Representative leaf with the honeycomb topology (*Berberis nervosa*) with cropped interior showing columnar intercellular airspaces (green) within the spongy mesophyll (S). The position of a representative stomate is indicated with a white arrow, showing spatial coordination with an adjacent column of intercellular airspace. Epidermis (E), palisade mesophyll (P), and vascular tissue (V) shown in grayscale. Scale bar = 50 µm. **(D)** Paradermal view of the same *B. nervosa* leaf's spongy mesophyll.

required for buoyancy (Fig. S1B). A distinctive third class of spongy mesophyll was observed in leaves with parallel venation (n = 4), in which strands of elongated mesophyll attached to veins at right angles, forming an approximately rectilinear lattice (Fig. S2).

Honeycomb mesophyll was composed of vertically stacked and horizontally aligned lattice layers. IAS columns formed by this alignment were typically positioned above stomata, forming conduits through the vertical profile of the leaf (Fig. 1C; Movies S1, S2). This supports the concept, suggested as early as 1914 by Haberlandt (*8*), that a primary function of the spongy mesophyll is to maximize CO_2 diffusion from stomata to the palisade, and provides insight into a longstanding question regarding the shape and size of the substomatal cavity (*18*, *19*). However, IAS connectivity was not strictly unidirectional. Rather, the vertical alignment of the individual mesophyll cell layers was often slightly offset or had gaps, which would allow for lateral diffusion of CO_2 between adjacent IAS columns (*20*, *21*).

To quantitatively examine the structure of the honeycomb spongy mesophyll (n = 29 species), we used the framework established by Gibson and Ashby (1999) for cellular solids (Data Set S1), for which honeycomb properties are derived from the packing scheme in the principal plane, i.e. the paradermal plane for plant leaves. Traits (Data Set S1) were measured on paradermal slices of spongy mesophyll (Fig. 2A,B) obtained via microCT imaging (Fig. 2C) and validated with fluorescence microscopy (Fig. 2D). At the cellular scale, the honeycomb structure was composed of cells with arm-like protrusions with a variety of individual morphologies (Fig. 2D). Yet, the tissue scale organization was largely invariant, highly ordered, and obeyed the topological constraints of Euler's Law (*17*), which governs how geometrical indices give rise to aggregate properties for continuous 2D honeycombs, and predicts the formation of hexagons from triply-joined vertices of a lattice. The most efficient honeycombs are hexagonal lattices, which minimize investment in materials needed to tessellate a 2D plane (*22*). Hexagonal honeycombs are characterized by their vertices that sit at the junction where edges meet, with a mean edge connectivity (Z_e) of three, a mean number of edges ($\bar{n}$) surrounding the hexagons of

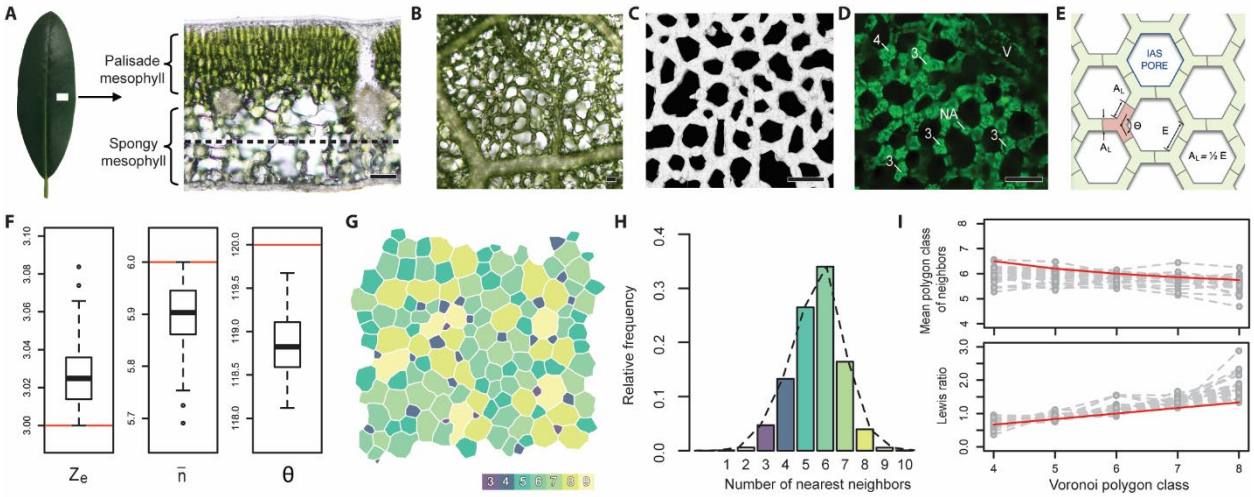

Fig. 2. Irregular honeycomb topology and structural characterization. (A) Cross-section of a representative leaf (*Rhododendron* sp. shown in panels A-D; scale bars = 50 µm). **(B)** Paradermal section showing spongy mesophyll tissue between veins. **(C)** MicroCT image of spongy mesophyll layer. **(D)** Fluorescence microscopy showing spongy mesophyll cell walls (dark lines) and chloroplasts (green). Cell arm counts (3, 4, NA) and vascular tissue (V) indicated. **(E)** Schematic diagram of honeycomb structure with cell walls (gray) outlining spongy mesophyll cells (tissue in green, individual cell in red) with arm length (A_L) and arm diameter (A_D). Arms form edges (E) that enclose intercellular airspace pores (IAS Pore) with internal angles (θ). **(F)** Box plots for mean edge connectivity (Z_e), mean edges per face ($\bar{n}$), and mean internal angle (θ) for n = 29 species with the honeycomb phenotype. Boxes represent inter-quartile range, lines across boxes represent group median, and whiskers extend from the upper and lower quartiles to the group maximum and minimum, respectively. Asterisks represent sample outliers. Red bars indicate values for a perfect hexagonal honeycomb. **(G)** Nearest neighbor diagram for a representative sample. **(H)** Frequency distribution of nearest neighbors for n = 29 species with the honeycomb phenotype. **(I)** Comparison of predicted (red) and measured (gray) values for dispersion in polygon properties for the Aboav-Weaire Law (upper panel) and Lewis' Rule (lower panel).

six, and a mean internal angle between edges (θ) of 120˚ (Fig. 2E). Across the species within our dataset, the spongy mesophyll tissue lattice had vertices that were joined by Z_e = 3.03 ± 0.02, the IAS was partitioned into polygons with $\bar{n}$ = 5.89 ± 0.07, and the characteristic θ of the IAS polygons was 118.86˚ ± 0.40˚ (Fig. 2F, Data Set S1). To quantify the degree of order in the structure, we calculated the tessellation entropy (*S*) for each sample, which would be zero for a perfectly ordered hexagonal honeycomb. We found a mean tessellation entropy of 1.43 ± 0.03, which is similar to values reported for irregular hexagonal honeycomb morphologies in engineered thin films (*S* = 1.48; *15*). We also found evidence for a distribution of IAS polygon sizes and classes (Figs. 2G,H) within the void space of the honeycomb lattice that satisfied

additional topological rules anticipated from a contiguous 2D honeycomb lattice. As given by the Aboav-Weaire Law (*24*) for neighboring polygon relationships, the occurrence of an IAS polygon with a lower than average number of edges ($n < 6$) introduced a corresponding polygon with a higher number of edges into the aggregate (Fig. 2I, upper panel). As expected from Lewis' Rule of polygon size dispersion (Figure 2I, lower panel), which is derived from the space filling properties of plant epithelial cells (*25*), the area of a given IAS polygon varied linearly with its number of edges. These data indicate that the spongy mesophyll and IAS matrix meet the assumptions for a hexagonal honeycomb with some irregularity as would be expected in a biological system (*17*) where multiple stresses act upon the structure throughout development. Taken together, these indices (Fig. 2F-I) show the applicability of the 2D honeycomb framework to spongy mesophyll tissue and provide insight into the dispersion of sizes and shapes of the IAS voids, which may provide insight for future work into the developmental processes by which the tissue was formed (*17*). We conclude that an irregular hexagonal honeycomb topology characterizes a common spongy mesophyll phenotype that spans a wide range of terrestrial plants, including representatives from the fern, gymnosperm, basal angiosperm (ANITA), magnoliid, and eudicot clades. The observation that some cells within the honeycomb lattice can be isodiametric while others have varying numbers of arm-like protrusions (Fig. 2D) implies that this structure may be formed by an arbitrary number of configurations of cell morphologies that, at the tissue scale, result in conservation of the global, ordered honeycomb topology governed by simple rules of cellular organization and optimality of resource allocation. Our data suggest that leaves with the honeycomb topology have optimized the construction of the spongy mesophyll to minimize cellular investment in a way that facilitates the vertical diffusion of CO_2 from the stomatal pore, through the spongy mesophyll layer, and into the palisade tissue where light is

most abundant for photosynthesis. This finding weakens the paradigm of spongy mesophyll as inherently disordered, and suggests that the emergent tissue structure is driven by conserved developmental (*26*), biomechanical, or functional requirements by certain laminar leaves, with distinct spongy mesophyll classes optimized for divergent physiological goals.

Drivers of phenotypic variation

To understand what factors were associated with variation in spongy mesophyll phenotype, random forest analysis was used to rank the importance of various anatomical, environmental, and taxonomic traits (Data Set S1) in classifying mesophyll as honeycomb (discretized IAS domains in the paradermal plane; Fig. 1C,D) or non-honeycomb (continuous IAS in the paradermal plane; Fig. 1A,B). Spongy mesophyll phenotype was best predicted by three anatomical traits (Fig. 3A): cell arm length (A_L), cell packing density, and the characteristic minimum vein spacing (see Supplementary Materials). Mesophyll classification showed steep transitional thresholds from honeycomb to non-honeycomb phenotypes at A_L values below ~12 µm (Fig. 3B), as cell packing density exceeded ~2000 cells mm^{-2} (Fig. 3C), and as minimum vein spacing fell below ~0.1 mm (Fig. 3D). Therefore, leaves with smaller, more densely packed spongy mesophyll cells and closely-spaced veins were more likely to have non-honeycomb topology with continuous IAS domains (n = 11 species), while leaves with fewer, larger cells per unit leaf area and more distantly spaced veins were more likely to exhibit the honeycomb topology with columnar airspace domains. The transition between phenotypes also corresponded with notable thresholds (Fig. S5) in vein density (D_v) and stomatal density (D_s). The non-honeycomb phenotype was associated with D_v above ~9 mm mm^{-2} and D_s above ~260 stomata mm^{-2}, which are trait values typically associated with angiosperm eudicots (*27*) and correlated

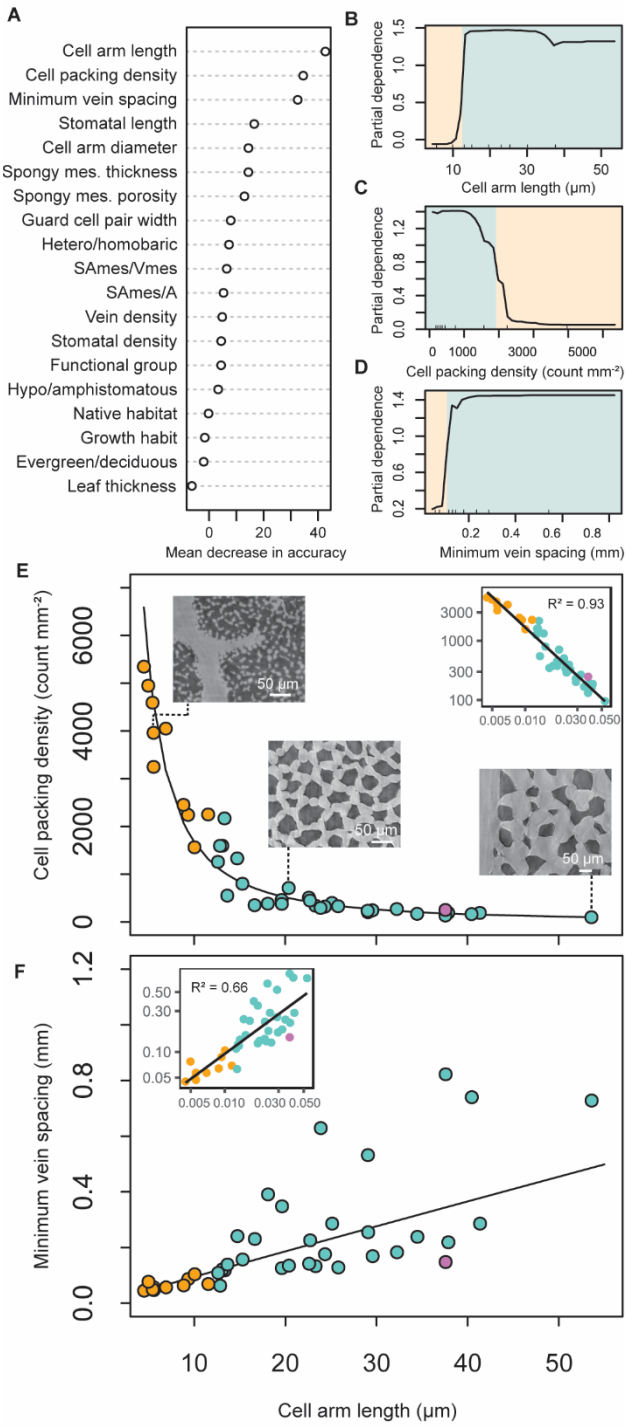

Fig. 3. Random forest classification of spongy mesophyll phenotypes. (A) Variable importance for classification between honeycomb and non-honeycomb phenotypes. Predictors at the top of the ranking have a higher relative importance in classification, as determined by mean decrease in accuracy when these variables are removed from the model. **(B-D)** Partial dependence plots showing logits (log fraction of votes) as a function of the three traits with highest relative importance. Blue shading shows approximate values over which probability favors the honeycomb phenotype; orange shading shows approximate values over which probability favors the non-honeycomb phenotype. **(E)** Power law relationship (solid line) between A_L and cell packing density; species with honeycomb and non-honeycomb spongy mesophyll are shown with blue and orange circles, respectively. *S. oleracea*, which was treated as non-honeycomb in the analysis yet had a unique phenotype, is indicated with a purple circle. Image insets demonstrate spongy mesophyll variation throughout the trait space. Figure inset shows the log-log transformed data and linear fit (solid line). **(F)** Power law relationship (solid line) between A_L and minimum vein spacing. Color scheme and figure inset are the same as in (E).

with high photosynthetic rates (*28*). Cell arm length was significantly correlated (Spearman correlation, r_s) with other leaf traits (Table S1), such that increases in cell arm length generally

reflected increases in the characteristic dimensions of the entire structure, e.g. cell arm diameter ($r_s = 0.95$, $p < 0.001$), stomatal guard cell length ($r_s = 0.78$, $p < 0.001$), and the diameter of the IAS voids in the honeycomb lattice ($r_s = 0.83$, $p < 0.001$).

With the indication that cell size, cell packing density, and vein spacing played an important role in phenotypic variation, we then explored the relationships between these traits. First, cell packing density was analyzed as a power law function of A_L ($R^2 = 0.93$, $F(1,38) = 520.2$, $P < 0.001$; Fig. 3E), which revealed the greatly amplified cell packing scheme in leaves with shorter cell arm length. In contrast, cell packing density was lower in species with long cell arms, which may reflect a lower number of cell divisions in the spongy mesophyll during development, thereby leading to greater stretching and cell elongation between adjacent cells in each monolayer, yielding longer cell arms at maturity (*29*). We note that cell counts taken from the transverse plane (as is typically done with light microscopy; *12*) would likely lead to overestimations. This might occur when cells have more articulated or more numerous arms, which could be counted as individual cells, confounding the patterns in space filling and cellular organization apparent in the paradermal plane.

An allometric scaling relationship was found between minimum vein spacing and A_L ($R^2 = 0.66$, $F(1,38) = 74$, $P < 0.001$, Fig. 3F), where eudicots with the shortest distances between veins had the smallest cells. This trend in consistent with previous work showing increasing investment in leaf veins and increased stomatal density, particularly in the flowering plants, over the past 125 million years as atmospheric CO_2 concentrations declined, which favored the optimization of the hydraulic and diffusional pathways in leaves, ultimately leading to higher photosynthetic rates (*27*, *28*, *30–32*). In terms of spongy mesophyll structure, this could point to the influence of veins in determining short-range order, where increasing vein density beyond a

critical threshold disrupts formation of the honeycomb topology. Leaf veins are typically located ~60% of the way through the leaf from the adaxial surface, near the transition between the palisade and spongy mesophyll (*6*); thus their physical influence during leaf development and cell arm elongation could contribute to the emergent irregular honeycomb topology that is not observed in the palisade mesophyll. Additionally, in terms of biomechanics, leaves with higher vein density have an abundance of semi-rigid xylem conduits that provide mechanical support (*27*). In contrast, the honeycomb structure itself could produce a lightweight material with rigidity in the in-plane direction, i.e. between both epidermises, and flexibility in the out of plane direction, i.e. transversally and longitudinally, much like manufactured honeycombs used in packing materials (*17*) and positioned between the upper and lower epidermises as in a sandwich structure (*33*).

Structural trait space scaling and functional implications

The spongy mesophyll structural trait space was best characterized by a power law relationship between the length and diameter of the cell arms ($R^2 = 0.81$, $F(1,35) = 148.3$, $P < 0.001$; Fig. 4A) with the honeycomb phenotype represented in gymnosperm (Fig. 4B), fern (Fig. 4C), ANITA (Fig. 4D), magnoliid (Fig. 4E), and eudicot (Fig. 4F) species, and the non-honeycomb phenotype only represented in eudicots (Fig. 4G). There were two notably unoccupied sectors of the trait space. First, no species in our dataset were found with large, isodiametric cells. Such a cell would have an extremely large volume, as found in succulent and epiphytic plants with recent 3D characterization (*16*, *34*). Such species may operate with a different biochemical pathway (CAM vs. C3), where large cell volume favors malic acid accumulation and water storage, as opposed to optimization of the mesophyll for C3 photosynthesis that prioritizes mesophyll conductance (*35*). The other sector of trait space

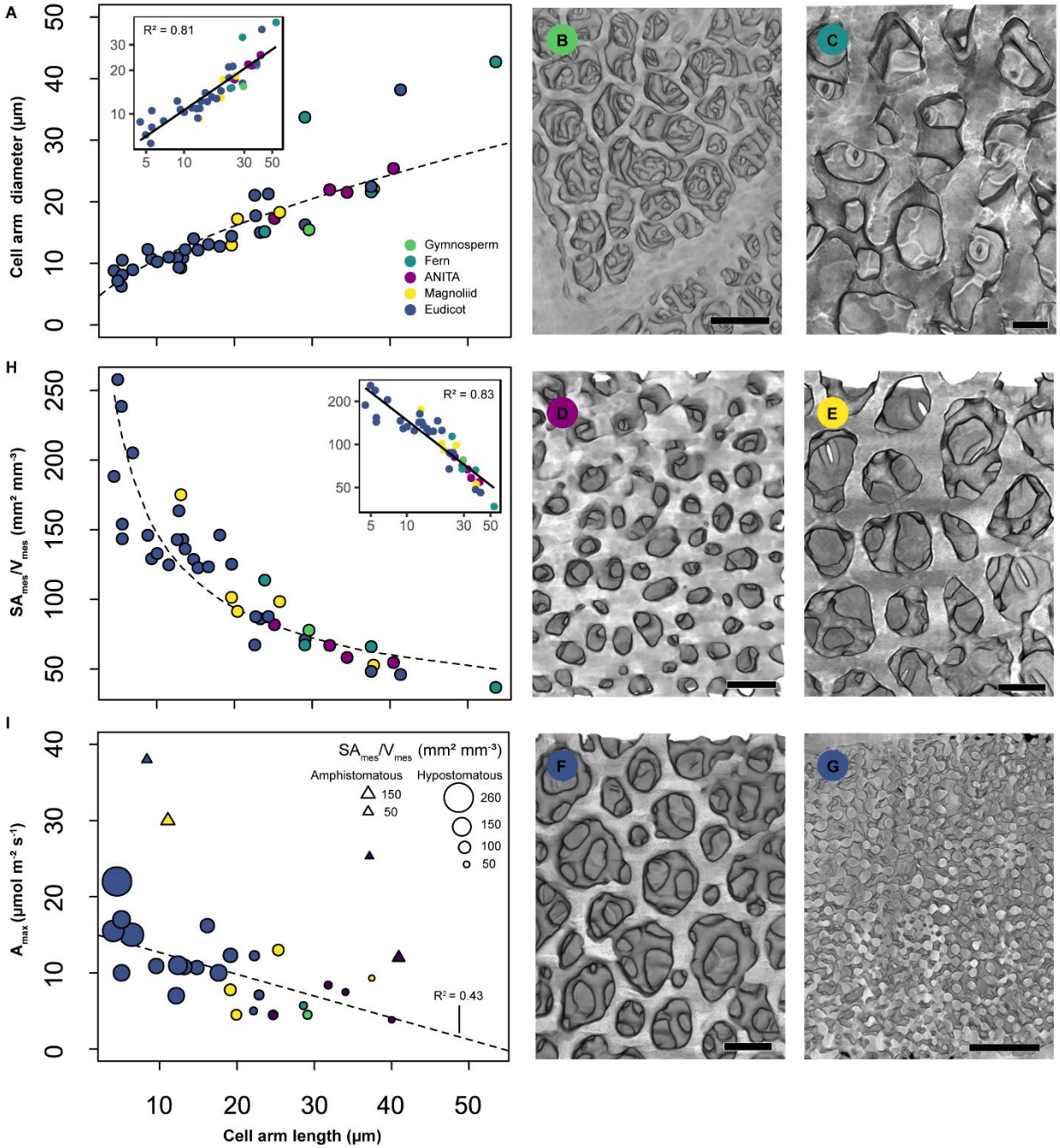

Fig. 4. Power law scaling of spongy mesophyll cell dimensions and models of derived photosynthetic properties. (A) Relationship between spongy mesophyll cell arm diameter (A_D) and arm length (A_L). Power law regression shown by the black dashed line. Inset shows log-log transformed data and linear fit (solid line). Colors represent sample phylogenetic affinity. **(B-G)** Spongy mesophyll structure viewed from the paradermal plane for representative species from gymnosperm (*Gnetum gnemon*, B), fern (*Platycerium andinum*, C), ANITA angiosperm (*Amborella trichopoda*, D), magnoliid (*Calycanthus occidentalis*, E), and eudicot (*Coffea arabica*, F; *Helianthus annuus*, G) clades. Scale bars = 50 µm. **(H)** Relationship between spongy mesophyll surface area to volume ratio (SA_{mes}/V_{mes}) and A_L. Power law regression shown by the black dashed line. Inset and colors scheme are the same as in **(A)**. **(I)** Linear relationship between A_{max} and A_L. Open circles represent hypostomatous species. Open triangles represent amphistomatous species, which were excluded from the regression. Point size scaled according to SA_{mes}/V_{mes}, which is linearly related to A_{max} ($R^2 = 0.62$). Colors represent sample phylogenetic affinity.

unoccupied by any of our study species was cells with highly elongated, narrow arms. This may be due to biomechanical limitations, or even to conserve a minimum distance between the nuclear envelope and the cell membrane for intracellular translocation.

To explore how spongy mesophyll structural traits predict photosynthetic properties of the leaf, we first modeled the spongy mesophyll cell surface area per unit tissue volume exposed to the intercellular airspace (SA_{mes}/V_{mes}) as a function of cell arm length. SA_{mes}/V_{mes} is a measure of the mesophyll surface area, i.e. evaporative and absorptive surface exposed to the IAS, and represents an intermediate step in the liquid-vapor pathway between veins and stomata. SA_{mes}/V_{mes}, is therefore a critical link between vein density and stomatal conductance in optimizing the hydraulic and diffusive pathways to increase leaf photosynthetic capacity (*36*). We found that as arm length increased, SA_{mes}/V_{mes} of the spongy mesophyll sharply decreased according to a power law ($R^2 = 0.83$, $F(1,38) = 188.7$, $P < 0.001$; Fig. 4A). Thus, plants with larger cells such as the fern *Platycerium andinum* (Fig. 4C), which were also more likely to exhibit the honeycomb phenotype, had highly reduced SA_{mes}/V_{mes} in the spongy mesophyll compared to eudicots with smaller cells and the non-honeycomb phenotype such as *Helianthus annuus* (sunflower, Fig. 4G). Although cell size strongly influenced SA_{mes}/V_{mes}, variation in cell geometry may also play a role (*14*, *15*), with lobed cells having more surface area than a spherical cell of the same volume. To demonstrate the implications for our dataset, we calculated SA_{mes}/V_{mes} for idealized geometrical models of isodiametric and triply-armed cells using measured cell arm lengths and diameters to parameterize the analysis (Fig. S6). As anticipated, surface area increased in triply-armed cells compared with isodiametric cells of the same volume, with a mean difference in SA_{mes}/V_{mes} between the two modeled cellular geometries of

0.069 $\mu m^2 \mu m^{-3}$ (s.d. = 0.029). This shows that, in addition to cell size and cell packing density, cell geometry is a mechanism for the regulation of SA_{mes}/V_{mes}.

Given that spongy mesophyll structure and surface area provide the physical basis for the conductance of CO_2 for photosynthesis, we lastly tested how leaf-level maximum photosynthetic rate (A_{max}) was related to A_L and SA_{mes}/V_{mes} of the spongy mesophyll (Fig. 1H). A_{max} decreased linearly with increasing A_L ($R^2 = 0.43$, $F(1,24) = 18.11$, $P < 0.001$; Fig. 4I). The highest A_{max} values were attributed primarily to species with non-honeycomb spongy mesophyll (Data Set S1), indicating a shift from lower to higher photosynthetic capacities as the leaf undergoes structural changes from honeycomb to non-honeycomb phenotypes. Species with amphistomatous leaves such as *H. annuus* and *Gossypium hirsutum* (cotton) were excluded from the model (shown in in Fig. 4I as open triangles), as the capacity for gas exchange on both sides of the leaf promotes higher photosynthetic rates (*37*). A_{max} increased linearly with increasing spongy mesophyll SA_{mes}/V_{mes} ($R^2 = 0.62$, $F(1,24) = 39.41$, $P < 0.001$; Fig. 4I); thus, although the palisade mesophyll is typically modeled with a higher photosynthetic capacity relative to the spongy mesophyll (*38*), there is a strong positive relationship between the quantity of photosynthetically active surface area per unit volume in the spongy mesophyll and leaf-level photosynthetic capacity.

Discussion

Given the historical dominance of 2D transverse analysis of leaves (Fig. 2A), our data highlight the importance of 3D characterization of leaf traits in determining mesophyll surface area (*5*, *15*); scaling relationships between morphological variation and tissue mass (*39*), and how tissue geometry influences the leaf economics spectrum (*40*). Investment in increased vein density and stomatal density allowed the angiosperms to optimize the leaf for maximum

photosynthetic rates, and these traits are apparently coordinated with a striking structural shift from the irregular honeycomb topology to the isodiametric non-honeycomb topological class. Our data suggest that cell size and cell packing are critical for the development of a spongy mesophyll structure optimized for high SA_{mes}/V_{mes}, and the absorptive surface for CO_2 acquisition (Fig. 4). Because cell size is fundamentally linked to genome size (*32*, *41*), streamlining the genome makes possible the miniaturization of xylem conduits, stomatal guard cells, and mesophyll cells, which collectively allow for higher photosynthetic capacity by optimizing the hydraulic and diffusive pathways in the leaf (*30*, *32*, *35*).

The widespread occurrence of the honeycomb topology suggests selection has favored minimizing cellular investment deep in the leaf where photosynthetic cells are often light limited. Honeycombs have been found widely in natural and engineered systems as multifunctional materials for fluid transport, energy conversion, and structural support (*42*). These patterns have been observed within different types of plant tissues, from epithelial cells (*43*) to the venation pattern of reticulate leaves (*44*) where a hexagonal honeycomb topology optimizes transport efficiency of the vascular system (*45*). Based on our dataset of dorsiventral leaves with reticulate venation, it also appears that the honeycomb form is hierarchically self-similar, where the spongy mesophyll repeats the pattern of the vasculature at a reduced scale. Thus, the same fundamental topology appears in multiple tissues and across scales within the plant, the honeycomb spongy mesophyll being a key representation. It is possible that the 3D honeycomb structure is driven by the physical processes and stresses that arise during development rather than functional constraints alone. Temporal and spatial coordination has been observed, for example, between mesophyll airspace and epidermal cell differentiation during development (*46*). However, we consider the hexagonal tessellation of the spongy mesophyll domain may be

the most efficient means of meeting multiple functional demands within a single tissue type; i.e. moving water over long distances outside the xylem, maintaining high diffusive conductance to CO_2, exporting the products of photosynthesis, and serving as a self-supporting structure when vein density is low. Hence, for plants with relatively large mesophyll cells, distantly spaced leaf veins, and moderate to low photosynthetic capacities, the emergent topological properties of the irregular hexagonal honeycomb structure provide an alternative strategy for resource allocation in the spongy mesophyll, a key trait dimension across the global spectrum of plant form (*47*). This work provides a new framework for exploring leaf form-function relationships, developmental processes, and physiological models in the 3D data era (*11*).

References and Notes:

1. C. K. Boyce, A. H. Knoll, Evolution of developmental potential and the multiple independent origins of leaves in Paleozoic vascular plants. *Paleobiology*. **28**, 70–100 (2002).

2. I. J. Wright, N. Dong, V. Maire, I. C. Prentice, M. Westoby, S. Díaz, R. V Gallagher, B. F. Jacobs, R. Kooyman, E. A. Law, M. R. Leishman, Ü. Niinemets, P. B. Reich, L. Sack, R. Villar, H. Wang, P. Wilf, Global climatic drivers of leaf size. *Science*. **357**, 917–921 (2017).

3. A. B. Nicotra, A. Leigh, C. K. Boyce, C. S. Jones, K. J. Niklas, D. L. Royer, H. Tsukaya, The evolution and functional significance of leaf shape in the angiosperms. *Funct. Plant Biol.* **38**, 535 (2011).

4. D. F. Parkhurst, Internal leaf structure: a three-dimensional perspective. *Econ. plant form Funct. Proc. Sixth Maria Moors Cabot Symp. Evol. Constraints Prim. Product. Adapt.*

Patterns Energy Capture Plants, Harvard For. August 1983 (1986).

5. G. Théroux-Rancourt, J. M. Earles, M. E. Gilbert, M. A. Zwieniecki, C. K. Boyce, A. J. McElrone, C. R. Brodersen, The bias of a two-dimensional view: comparing two-dimensional and three-dimensional mesophyll surface area estimates using noninvasive imaging. *New Phytol.* **215**, 1609–1622 (2017).

6. A. M. Borsuk, C. R. Brodersen, The Spatial Distribution of Chlorophyll in Leaves. *Plant Physiol.* **180**, 1406–1417 (2019).

7. Q. T. Ho, H. N. C. Berghuijs, R. Watté, P. Verboven, E. Herremans, X. Yin, M. A. Retta, B. Aernouts, W. Saeys, L. Helfen, G. D. Farquhar, P. C. Struik, B. M. Nicolaï, Three-dimensional microscale modelling of CO2 transport and light propagation in tomato leaves enlightens photosynthesis. *Plant. Cell Environ.* **39**, 50–61 (2016).

8. G. Haberlandt, *Physiological Plant Anatomy* (Macmillan and Co., London, 1914).

9. W. K. Smith, T. C. Vogelmann, E. H. Delucia, D. T. Bell, K. A. Shepherd, Leaf Form and Photosynthesis: Do leaf structure and orientation interact to regulate internal light and carbon dioxide? *Source Biosci.* **47**, 785–793 (1997).

10. I. Terashima, Y. T. Hanba, D. Tholen, U. Niinemets, Leaf Functional Anatomy in Relation to Photosynthesis. *Plant Physiol.* **155**, 108–16 (2011).

11. J. M. Earles, T. N. Buckley, C. R. Brodersen, F. A. Busch, F. J. Cano, B. Choat, J. R. Evans, G. D. Farquhar, R. Harwood, M. Huynh, G. P. John, M. L. Miller, F. E. Rockwell, L. Sack, C. Scoffoni, P. C. Struik, A. Wu, X. Yin, M. M. Barbour, Embracing 3D Complexity in Leaf Carbon–Water Exchange. *Trends Plant Sci.* (2018).

12. R. B. Wylie, Cicatrization of Foliage Leaves II. Wound Responses of Certain Broad-

Leaved Evergreens. *Bot. Gaz.* **92**, 279–295 (1931).

13. R. B. Wylie, Principles of Foliar Organization Shown by Sun-Shade Leaves from Ten Species of Deciduous Dicotyledonous Trees. *Am. J. Bot.* **38**, 355 (1951).

14. L. A. Ivanova, V. I. P'yankov, Structural adaptation of the leaf mesophyll to shading. *Russ. J. Plant Physiol.* **49**, 419–431 (2002).

15. R. Harwood, E. Goodman, M. Gudmundsdottir, M. Huynh, Q. Musulin, M. Song, M. M. Barbour, *New Phytol.*, in press, doi:10.1111/nph.16219.

16. J. Earles, G. Théroux-Rancourt, A. Roddy, M. Gilbert, A. McElrone, C. Brodersen, Beyond porosity: 3D leaf intercellular airspace traits that impact mesophyll conductance. *Plant Physiol.* (2018).

17. L. J. Gibson, M. F. Ashby, *Cellular solids: structure and properties* (Cambridge university press, 1999).

18. W. F. Pickard, Why is the substomatal chamber as large as it is? *Plant Physiol.* **69**, 971–4 (1982).

19. D. F. Parkhurst, S. C. Wong, G. D. Farquhar, I. R. Cowan, Gradients of Intercellular CO2 Levels Across the Leaf Mesophyll. *Plant Physiol.* **86**, 1032–7 (1988).

20. R. Pieruschka, U. Schurr, M. Jensen, W. F. Wolff, S. Jahnke, Lateral diffusion of CO2 from shaded to illuminated leaf parts affects photosynthesis inside homobaric leaves. *New Phytol.* **169**, 779–788 (2006).

21. J. Morison, T. Lawson, Does lateral gas diffusion in leaves matter? *Plant. Cell Environ.* **30**, 1072–1085 (2007).

22. T. C. Hales, The honeycomb conjecture. *Discret. Comput. Geom.* **25**, 1–22 (2001).

23. T. Pietsch, N. Gindy, A. Fahmi, Nano- and micro-sized honeycomb patterns through hierarchical self-assembly of metal-loaded diblock copolymer vesicles. *Soft Matter*. **5**, 2188–2197 (2009).

24. D. Weaire, Some remarks on the arrangement of grains in a polycrystal. *Metallography*. **7**, 157–160 (1974).

25. F. T. Lewis, The correlation between cell division and the shapes and sizes of prismatic cells in the epidermis of cucumis. *Anat. Rec.* **38**, 341–376 (1928).

26. E. Panteris, B. Galatis, The morphogenesis of lobed plant cells in the mesophyll and epidermis: organization and distinct roles of cortical microtubules and actin filaments. *New Phytol.* **167**, 721–732 (2005).

27. L. Sack, C. Scoffoni, Leaf venation: Structure, function, development, evolution, ecology and applications in the past, present and future. *New Phytol.* **198** (2013), pp. 983–1000.

28. T. J. Brodribb, T. S. Feild, G. J. Jordan, Leaf maximum photosynthetic rate and venation are linked by hydraulics. *Plant Physiol.* **144**, 1890–1898 (2007).

29. G. S. Avery, Structure and development of the tobacco leaf. *Am. J. Bot.* **20**, 565–592 (1933).

30. H. J. de Boer, M. B. Eppinga, M. J. Wassen, S. C. Dekker, A critical transition in leaf evolution facilitated the Cretaceous angiosperm revolution. *Nat. Commun.* **3**, 1221 (2012).

31. J. Gago, M. Carriquí, M. Nadal, M. J. Clemente-Moreno, R. E. Coopman, A. R. Fernie, J. Flexas, Photosynthesis Optimized across Land Plant Phylogeny. *Trends Plant Sci.* **0** (2019).

32. K. A. Simonin, A. B. Roddy, Genome downsizing, physiological novelty, and the global dominance of flowering plants. *PLOS Biol.* **16**, e2003706 (2018).

33. L. J. Gibson, M. F. Ashby, K. E. Easterling, Structure and mechanics of the iris leaf. *J. Mater. Sci.* **23**, 3041–3048 (1988).

34. E. A. Nelson, R. F. Sage, Functional constraints of CAM leaf anatomy: tight cell packing is associated with increased CAM function across a gradient of CAM expression. *J. Exp. Bot.* **59**, 1841–1850 (2007).

35. J. Gago, M. Carriquí, M. Nadal, M. J. Clemente-Moreno, R. E. Coopman, A. R. Fernie, J. Flexas, Photosynthesis Optimized across Land Plant Phylogeny. *Trends Plant Sci.* **24**, 947–958 (2019).

36. C. Scoffoni, D. S. Chatelet, J. Pasquet-Kok, M. Rawls, M. J. Donoghue, E. J. Edwards, L. Sack, Hydraulic basis for the evolution of photosynthetic productivity. *Nat. Plants*. **2** (2016).

37. C. D. Muir, Is Amphistomy an Adaptation to High Light? Optimality Models of Stomatal Traits along Light Gradients. *Integr. Comp. Biol.* **59**, 571–584 (2019).

38. Q. T. Ho, H. N. C. Berghuijs, R. Watté, P. Verboven, E. Herremans, X. Yin, M. A. Retta, B. Aernouts, W. Saeys, L. Helfen, G. D. Farquhar, P. C. Struik, B. M. Nicolaï, Three-dimensional microscale modelling of CO2 transport and light propagation in tomato leaves enlightens photosynthesis. *Plant. Cell Environ.* **39**, 50–61 (2016).

39. C. A. Price, B. J. Enquist, Scaling mass and morphology in leaves: an extension of the WBE model. *Ecology*. **88**, 1132–1141 (2007).

40. I. J. Wright, P. B. Reich, M. Westoby, D. D. Ackerly, Z. Baruch, F. Bongers, J. Cavender-

Bares, T. Chapin, J. H. C. Cornelissen, M. Diemer, J. Flexas, E. Garnier, P. K. Groom, J. Gulias, K. Hikosaka, B. B. Lamont, T. Lee, W. Lee, C. Lusk, J. J. Midgley, M.-L. Navas, Ü. Niinemets, J. Oleksyn, N. Osada, H. Poorter, P. Poot, L. Prior, V. I. Pyankov, C. Roumet, S. C. Thomas, M. G. Tjoelker, E. J. Veneklaas, R. Villar, The worldwide leaf economics spectrum. *Nature*. **428**, 821–827 (2004).

41. A. B. Roddy, G. Théroux-Rancourt, T. Abbo, J. W. Benedetti, C. R. Brodersen, M. Castro, S. Castro, A. B. Gilbride, B. Jensen, G.-F. Jiang, J. A. Perkins, S. D. Perkins, J. Loureiro, Z. Syed, R. A. Thompson, S. E. Kuebbing, K. A. Simonin, The Scaling of Genome Size and Cell Size Limits Maximum Rates of Photosynthesis with Implications for Ecological Strategies. *Int. J. Plant Sci.* (2019), doi:10.1086/706186.

42. Q. Zhang, X. Yang, P. Li, G. Huang, S. Feng, C. Shen, B. Han, X. Zhang, F. Jin, F. Xu, T. J. Lu, Bioinspired engineering of honeycomb structure – Using nature to inspire human innovation. *Prog. Mater. Sci.* **74**, 332–400 (2015).

43. F. T. Lewis, The correlation between cell division and the shapes and sizes of prismatic cells in the epidermis of cucumis. *Anat. Rec.* **38**, 341–376 (1928).

44. C. A. Price, S. Wing, J. S. Weitz, Scaling and structure of dicotyledonous leaf venation networks. *Ecol. Lett.* **15**, 87–95 (2012).

45. L. Fiorin, T. J. Brodribb, T. Anfodillo, Transport efficiency through uniformity: Organization of veins and stomata in angiosperm leaves. *New Phytol.* **209**, 216–227 (2016).

46. M. R. Lundgren, A. Mathers, A. L. Baillie, J. Dunn, M. J. Wilson, L. Hunt, R. Pajor, M. Fradera-Soler, S. Rolfe, C. P. Osborne, C. J. Sturrock, J. E. Gray, S. J. Mooney, A. J.

Fleming, Mesophyll porosity is modulated by the presence of functional stomata. *Nat. Commun.* **10**, 2825 (2019).

47. S. Díaz, J. Kattge, J. H. C. Cornelissen, I. J. Wright, S. Lavorel, S. Dray, B. Reu, M. Kleyer, C. Wirth, I. Colin Prentice, E. Garnier, G. Bönisch, M. Westoby, H. Poorter, P. B. Reich, A. T. Moles, J. Dickie, A. N. Gillison, A. E. Zanne, J. Chave, S. Joseph Wright, S. N. Sheremet Ev, H. Jactel, C. Baraloto, B. Cerabolini, S. Pierce, B. Shipley, D. Kirkup, F. Casanoves, J. S. Joswig, A. Günther, V. Falczuk, N. Rüger, M. D. Mahecha, L. D. Gorné, The global spectrum of plant form and function. *Nature*. **529**, 167–171 (2016).

48. J. Schindelin, I. Arganda-Carreras, E. Frise, V. Kaynig, M. Longair, T. Pietzsch, S. Preibisch, C. Rueden, S. Saalfeld, B. Schmid, J.-Y. Tinevez, D. J. White, V. Hartenstein, K. Eliceiri, P. Tomancak, A. Cardona, Fiji: an open-source platform for biological-image analysis. *Nat. Methods*. **9**, 676–82 (2012).

49. L. Sack, C. Scoffoni, A. D. McKown, K. Frole, M. Rawls, J. C. Havran, H. Tran, T. Tran, Developmentally based scaling of leaf venation architecture explains global ecological patterns. *Nat. Commun.* **3**, 837 (2012).

50. C. K. Boyce, Seeing the forest with the leaves - Clues to canopy placement from leaf fossil size and venation characteristics. *Geobiology*. **7**, 192–199 (2009).

51. C. K. Boyce, T. J. Brodribb, T. S. Feild, M. A. Zwieniecki, Angiosperm leaf vein evolution was physiologically and environmentally transformative. *Proc. R. Soc. B Biol. Sci.* **276**, 1771–1776 (2009).

52. T. J. Brodribb, T. S. Feild, Leaf hydraulic evolution led a surge in leaf photosynthetic capacity during early angiosperm diversification. *Ecol. Lett.* **13**, 175–183 (2010).

53. R. L. Walls, Angiosperm leaf vein patterns are linked to leaf functions in a global-scale data set. *Am. J. Bot.* **98**, 244–253 (2011).

54. A. Nardini, E. Õunapuu-Pikas, T. Savi, When smaller is better: Leaf hydraulic conductance and drought vulnerability correlate to leaf size and venation density across four Coffea arabica genotypes. *Funct. Plant Biol.* **41**, 972–982 (2014).

55. T. S. Feild, L. Balun, Xylem hydraulic and photosynthetic function of Gnetum (Gnetales) species from Papua New Guinea. *New Phytol.* **177**, 665–675 (2008).

56. V. Amiard, K. E. Mueh, B. Demmig-Adams, V. Ebbert, R. Turgeon, W. W. Adams, Anatomical and photosynthetic acclimation to the light environment in species with differing mechanisms of phloem loading. *Proc. Natl. Acad. Sci. U. S. A.* **102**, 12968–12973 (2005).

57. C. R. Brodersen, T. C. Vogelmann, W. E. Williams, H. L. Gorton, A new paradigm in leaf-level photosynthesis: Direct and diffuse lights are not equal. *Plant, Cell Environ.* **31**, 159–164 (2008).

58. Z. Lu, J. Chen, R. G. Percy, E. Zeiger, Photosynthetic rate, stomatal conductance and leaf area in two cotton species (Gossypium barbadense and Gossypium hirsutum) and their relation with heat resistance and yield. *Aust. J. Plant Physiol.* **24**, 693–700 (1997).

59. A. W. Fellows, M. L. Goulden, Controls on gross production by a semiarid forest growing near its warm and dry ecotonal limit. *Agric. For. Meteorol.* **169**, 51–60 (2013).

60. K. A. Martinez, J. D. Fridley, Acclimation of leaf traits in seasonal light environments: Are non-native species more plastic? *J. Ecol.* **106**, 2019–2030 (2018).

61. R. T. Olsen, J. M. Ruter, M. W. Rieger, Photosynthetic Responses of Container-grown

Illicium L. Taxa to Sun and Shade. *J. Am. Soc. Hortic. Sci.* **127**, 919–924 (2002).

62. J. R. Stewart, R. D. Landes, A. K. Koeser, A. L. Pettay, Net photosynthesis and growth of three novel woody species under water stress: Calycanthus occidentalis, Fraxinus anomala, and Pinckneya pubens. *HortScience*. **42**, 1341–1345 (2007).

63. K. Batista, M. E. Loureiro, C. Ducatti, Growth and photosynthetic down-regulation in Coffea arabica in response to restricted root volume. *Artic. Funct. Plant Biol.* (2006).

64. S. Takahashi, A. Tamashiro, Y. Sakihama, Y. Yamamoto, Y. Kawamitsu, H. Yamasaki, High-susceptibility of photosynthesis to photoinhibition in the tropical plant Ficus microcarpa L. f. cv. Golden Leaves. *BMC Plant Biol.* **2** (2002).

65. C. H. Lusk, A. Del Pozo, Survival and growth of seedlings of 12 Chilean rainforest trees in two light environments: Gas exchange and biomass distribution correlates. *Austral Ecol.* **27**, 173–182 (2002).

66. T. S. Feild, N. C. Arens, T. E. Dawson, The ancestral ecology of angiosperms: Emerging perspectives from extant basal lineages. *Int. J. Plant Sci.* **164** (2003).

67. D. Greer, M. Weedon, Modelling photosynthetic responses to temperature of grapevine (Vitis vinifera cv. Semillon) leaves on vines grown in a hot climate. *Plant. Cell Environ.* **35**, 1050–1064 (2012).

68. L.-S. Chen, L. Cheng, "Carbon Assimilation and Carbohydrate Metabolism of 'Concord' Grape (Vitis labrusca L.) Leaves in Response to Nitrogen Supply" (2003).

69. M. Vaz, J. S. Pereira, L. C. Gazarini, T. S. David, J. S. David, A. Rodrigues, J. Maroco, M. M. Chaves, Drought-induced photosynthetic inhibition and autumn recovery in two Mediterranean oak species (Quercus ilex and Quercus suber). *Tree Physiol.* **30**, 946–956

(2010).

70. D. S. Chatelet, W. L. Clement, L. Sack, M. J. Donoghue, E. J. Edwards, The evolution of photosynthetic anatomy in Viburnum (Adoxaceae). *Int. J. Plant Sci*. **174**, 1277–1291 (2013).

71. Z. P. Ye, Q. Yu, H. J. Kang, Evaluation of photosynthetic electron flow using simultaneous measurements of gas exchange and chlorophyll fluorescence under photorespiratory conditions. *Photosynthetica*. **50**, 472–476 (2012).

72. W. Martindale, R. C. Leegood, Acclimation of photosynthesis to low temperature in Spinacia oleracea L. II. Effects of nitrogen supply . *J. Exp. Bot.* **48**, 1873–1880 (1997).

73. R. Thomas Fernandez, R. E. Schutzki, K. J. Prevete, Influence of Spring and Fall Drought Stresses on Growth and Gas Exchange during Stress and Posttransplant of Container-grown Magnolia ×soulangiana "Jane." *J. Am. Soc. Hortic. Sci.* **127**, 38–44 (2002).

74. E. Kaiser, A. Morales, J. Harbinson, E. Heuvelink, A. E. Prinzenberg, L. F. M. Marcelis, Metabolic and diffusional limitations of photosynthesis in fluctuating irradiance in Arabidopsis thaliana. *Sci. Rep.* **6** (2016).

75. A. J. McElrone, I. N. Forseth, Photosynthetic Responses of a Temperate Liana to Xylella fastidiosa Infection and Water Stress. *J. Phytopathol.* **152**, 9–20 (2004).

76. M. Doube, M. M. Kłosowski, I. Arganda-Carreras, F. P. Cordelières, R. P. Dougherty, J. S. Jackson, B. Schmid, J. R. Hutchinson, S. J. Shefelbine, BoneJ: Free and extensible bone image analysis in ImageJ. *Bone*. **47**, 1076–1079 (2010).

77. R Core Team, R: A language and environment for statistical computing (2018), p. Vienna, Austria. URL https://www.r-project.org/.

78. F. de Chaumont, S. Dallongeville, N. Chenouard, N. Hervé, S. Pop, T. Provoost, V. Meas-Yedid, P. Pankajakshan, T. Lecomte, Y. Le Montagner, T. Lagache, A. Dufour, J.-C. Olivo-Marin, Icy: an open bioimage informatics platform for extended reproducible research. *Nat. Methods*. **9**, 690–696 (2012).

79. D. Heller, A. Hoppe, S. Restrepo, L. Gatti, A. L. Tournier, N. Tapon, K. Basler, Y. Mao, EpiTools: An Open-Source Image Analysis Toolkit for Quantifying Epithelial Growth Dynamics. *Dev. Cell*. **36**, 103–116 (2016).

80. A. Liaw, M. Wiener, Classification and regression by randomForest. *R news*. **2**, 18–22 (2002).

Acknowledgments: We thank Professor Lorna Gibson (Massachusetts Institute of Technology) for discussion, and Professor Tim Brodribb (University of Tasmania) and Professor Erika Edwards (Yale University) for providing feedback on a draft manuscript. We additionally thank the Marsh Botanical Garden (New Haven, CT), the University of California Botanical Garden (Berkeley, CA), the UC Davis Botanical Conservatory (Davis, CA), and the UC Davis Arboretum (Davis, CA) for plant material, and Kyra Prats (Yale University) for assistance with maximum photosynthetic rate data collection. GTR acknowledges the Paul Scherrer Institut, Villigen, Switzerland for provision of synchrotron radiation beamtime at beamline TOMCAT.

Funding: This material is based upon work supported by the National Science Foundation Graduate Research Fellowship Program under Grant No. DGE1752134. Any opinions, findings, and conclusions or recommendations expressed in this material are those of the author(s) and do not necessarily reflect the views of the National Science Foundation. The Advanced Light Source is supported by the Director, Office of Science, Office of Basic Energy Sciences, of the

US Department of Energy under Contract no. DE-AC02-05CH11231. GTR was supported by the Austrian Science Fund (FWF), project no. M2245. **Author contributions:** A.M.B. conceived of the original research plan and jointly with C.R.B. designed the methods, acquired, analyzed, and interpreted the data, and drafted and revised the manuscript. A.B.R. acquired leaf microCT data and contributed to data analysis and manuscript revision. G.T.R. acquired leaf microCT data and contributed to manuscript revision. **Competing interests:** The authors declare no competing interests. **Data and materials availability:** All data is available in the manuscript or the supplementary materials.

Supplementary Materials:

Materials and Methods

Figure S1-S6

Tables S1-S3

Movies S1-S2

References (*17*, *22*, *50–59*, *23*, *60–69*, *24*, *70–79*, *25*, *80*, *27*, *28*, *36*, *48*, *49*)